Article

Reduction of (100)-Faceted CeO$_2$ for Effective Pt Loading

Akira Yoko,* Haodong Wang, Ko Furuya, Daiki Takahashi, Gimyeong Seong, Takaaki Tomai, Anatoly I. Frenkel,* Mitsuhiro Saito, Kazutoshi Inoue, Yuichi Ikuhara,* and Tadafumi Adschiri*

Read Online

ACCESS | Metrics & More | Article Recommendations | Supporting Information

ABSTRACT: Although the function and stability of catalysts are known to significantly depend on their dispersion state and support interactions, the mechanism of catalyst loading has not yet been elucidated. To address this gap in knowledge, this study elucidates the mechanism of Pt loading based on a detailed investigation of the interaction between Pt species and localized polarons (Ce^{3+}) associated with oxygen vacancies on CeO$_2$(100) facets. Furthermore, an effective Pt loading method was proposed for achieving high catalytic activity while maintaining the stability. Enhanced dispersibility and stability of Pt were achieved by controlling the ionic interactions between dissolved Pt species and CeO$_2$ surface charges via pH adjustment and reduction pretreatment of the CeO$_2$ support surface. This process resulted in strong interactions between Pt and the CeO$_2$ support. Consequently, the oxygen-carrier performance was improved for CH$_4$ chemical looping reforming reactions. This simple interaction-based loading process enhanced the catalytic performance, allowing the efficient use of noble metals with high performance and small loading amounts.
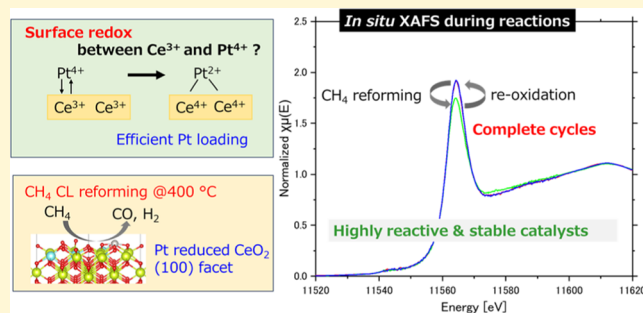
INTRODUCTION

Noble metals, such as Pt, Ru, Rh, Pd, Ag, and Au, dispersed on metal-oxide supports are widely used as catalysts in various reactions, including CO oxidation, selective hydrogenation, selective hydrodeoxygenation, C−C coupling, N$_2$O decomposition, CH$_4$ dry reforming, CO$_2$ electroreduction, H$_2$O$_2$ sensing, hydroformylation, amination, and water dissociation.[1−12] Among the various metal oxides available, CeO$_2$ is an important support material because it serves as an oxygen reservoir with high storage capacity.[13−16] By depositing noble metals onto the CeO$_2$ surface, the surface reactivity of oxygen can be enhanced, resulting in high oxygen usability at low temperatures.[13−16] These factors enable chemical looping reactions, where two reactions are conducted alternately in different reactors.[17] Gaseous products can be recovered separately using the chemical looping method, leading to increased reaction efficiency.[17] Although it is widely known that the function and stability of catalysts depend greatly on their dispersion state and support interactions, the mechanism of catalyst loading has not been investigated in detail.[18]

Given the scarcity of noble metals, the efficient preparation of catalysts by using these elements is crucial. Recently, single-atom catalysts (SACs) have received considerable attention[18−20] because, in addition to the dispersibility of noble metals, their interactions with the metal-oxide support are key to achieving high reactivity and stability. For instance, stronger interactions between Pt and the CeO$_2$(100) facet have been observed than those between Pt and other facets.[21] In addition, dynamic charge and oxidation state of Pt on CeO$_2$(100) were

theoretically discussed.[22] However, the control and identification of stable facets remain challenging. Furthermore, the interaction of Pt with Ce^{3+} ions associated with oxygen vacancies (V$_O$) is characteristic for Pt/SACs, as demonstrated in a study on aliovalent metal-doped CeO$_2$.[23−25] An improved understanding of these interactions is important for elucidating reaction mechanisms and ensuring high catalytic performance. Recently, dynamics of the Pt under reduction treatment of Pt/SACs CeO$_2$ has also been reported.[26,27]

Significant advances have been made in synthesizing CeO$_2$ nanocrystals and understanding their unique chemical states.[28−31] Additionally, controlled synthesis of CeO$_2$ nanocubes with exposed (100) facets has been achieved using the supercritical hydrothermal method.[28−32] The (100) facet is an unstable surface with high surface energy and reactivity, affording high oxygen-storage capacity at low temperatures (<300 °C).[29−36] This is unusual compared with ordinary CeO$_2$ particles with exposed (111) facets. The chemical activity of CeO$_2$(100) nanocubes is strongly dependent on particle size. Hence, extremely high activity and reducibility can be achieved by precisely controlling their size.[30,31] The reduced surface states of CeO$_2$(100) nanocubes have been clearly visualized in

previous studies, which demonstrated a remarkably high Ce^{3+} concentration on the surface.[30,31] Thus, $CeO_2(100)$ is a highly promising support surface for noble-metal-loaded solid catalysts and oxygen carriers.[34,36] In particular, interactions between noble-metal species and $CeO_2(100)$ nanocube surfaces are expected to differ from those of ordinary bulk CeO_2 surfaces.

In this study, the interaction between Pt and reduced CeO_2 nanoparticles with exposed (100) facets was examined to develop a highly dispersed catalytic loading method that utilizes the redox properties of CeO_2. A previous study[21] demonstrated the high affinity between the $CeO_2(100)$ surface and Pt, suggesting that remarkably high reactivity and stability can be obtained for Pt dispersed on the (100) facets of precisely controlled CeO_2 nanocubes. The highly reduced nature of the (100) facets[30,31] facilitated the analysis of interactions between Pt and Ce^{3+} or oxygen vacancies. During the deposition process, promising electron transfer was observed between Pt cations and the reduced CeO_2 surface, facilitating a strong interaction. Pt loading on oxidized or reduced $CeO_2(100)$ surfaces was studied, and an efficient loading method was developed. Chemical looping methane reforming was studied as a model reaction system, and the obtained Pt−CeO_2 was found to be a high-performing oxygen carrier. Chemical looping is a promising reaction scheme with high efficiency, particularly for the separate recovery of gaseous products owing to the oxygen-carrying capability of metal oxides. Hence, the development of suitable low-temperature oxygen carriers is vital.

■ METHODS

Materials. CeO_2 nanocubes modified with decanoic acid were synthesized by a continuous hydrothermal process.[37] Post synthesis, these particles were dried using supercritical CO_2 to prevent aggregation (ITEC Co., Ltd., Japan).[38] $H_2PtCl_6·6H_2O$ (Fujifilm Wako Pure Chemical Corp., Japan) was used as the Pt precursor, and distilled water was obtained by using an Auto Still water purification system (WG250; Yamato Scientific Co., Ltd.).

Preparation of Pt−CeO_2. The synthesized organic-modified CeO_2 nanoparticles were calcined in the air at 300 °C for 2 h to remove the modifier on the surface as established before.[28,33] The obtained particles are termed oxidized CeO_2. These oxidized particles were then subjected to a reducing atmosphere of 7% H_2/Ar at 400 °C for 2 h, providing reduced CeO_2 based on the previous study.[39] Pt deposition was conducted on both oxidized and reduced CeO_2. For this, CeO_2 was dispersed by sonication for 1 h in an aqueous solution. The mixture of CeO_2 and the H_2PtCl_6 solution was stirred at 1000 rpm for 1 h at 60 °C while maintaining a pH of 3. After centrifugation and washing, the particles were freeze-dried and then calcined again at 300 °C for 12 h in the air.

Characterization Methods. ζ potentials of the CeO_2 nanoparticles were measured by a laser Doppler electrophoresis method at 25 °C (Zetasizer Nano ZS equipped with a titrator (MPT-2), Malvern Panalytical). The morphologies of the products were examined using field-emission scanning transmission electron microscopy (STEM; JEM-ARM200F; JEOL Ltd.). Electron energy loss spectroscopy (EELS) was performed in the line-scanning mode, and Ce M-edge spectra were recorded for each atomic column. The product compositions after acidic dissolution were determined using inductively coupled plasma atomic emission spectroscopy (ICP-AES; ARCOS FHM22 MV130, Spectro Analytical Instruments, Ametek Inc.). X-ray photoelectron spectroscopy (XPS; PHI5000 Versa Probe II, ULVAC-PHI, Inc.) was performed using Al Kα (1486.6 eV) X-rays generated at 15 kV and 25 W, with a beam size of 200 μm. For recording the Pt 4f spectra, the measurement time step was 20 ms, and the energy step was 0.1 eV. During the measurement,

charge neutralization was conducted with Ar ion sputtering. Synchrotron X-ray absorption fine structure (XAFS) data were obtained at beamline 7-BM of National Synchrotron Light Source-II (NSLS-II) at Brookhaven National Laboratory. For the in situ experiments, oxygen (20% He diluted) and CH_4 (100%) were introduced alternately. At each interval, He was used for gas replacement, and the XAFS data were obtained by using a fluorescence detector positioned at 45° angle with respect to the X-ray beam direction. A high-temperature Nashner-Adler cell was used, and the samples were pelletized without dilution. Pt L_3-edge XAFS spectra were recorded during the reaction. Diffuse reflectance infrared Fourier Transform spectroscopy (DRIFTS) measurements were conducted while increasing the temperature to 300 °C while feeding CO or He to observe the CO adsorption or desorption patterns. Methane reactions were conducted using a catalyst analyzer (BELCAT-II, MicrotracBEL), with ∼50 mg of the powder sample loaded and heated to 400 °C with 20% oxygen (diluted with Ar). After oxidation for 20 min, the reaction involving gas replacement with Ar was conducted for 15 min, and a reaction with 67% CH_4 (diluted with Ar) was conducted for 60 min. The entire reaction was performed twice. The produced gas was detected by mass spectrometry (MS, BELMASS, MicrotracBEL) at the outlet.

The surface states were simulated via DFT using the Vienna Ab initio Simulation Package (VASP) code,[40,41] and the generalized gradient approximation (GGA)[42] proposed by Perdew et al. was employed as the exchange-correlation energy functional. The DFT + U method[43] introduced by Dudarev et al. was used to treat electron localization. The $U−J$ parameter was set at 5.0 eV for Ce 4f, 7.5 eV for Pt 5d, and 5.5 eV for O 2p, in accordance with previous studies on CeO_2[44] and PtO_2.[45] The valence configurations of the pseudopotentials were $5s^2 5p^6 4f^1 5d^1 6s^2$ for Ce, $5p^6 5d^9 6s^1$ for Pt, and $2s^2 2p^4$ for O. The energy cutoff for the plane-wave basis was set at 500 eV for all calculations, with a Monkhorst−Pack k-point mesh size of $2 \times 2 \times 1$. Dipole correction implemented in VASP was employed.[46,47] The (100) slab model with 192 atoms ($2 \times 2 \times 4$ times of the unit cell) was used as the surface model. The forces converged to <0.02 eV/Å in all the calculations. The calculated atomic configuration models were visualized using the VESTA code.[48]

■ RESULTS AND DISCUSSION

Adsorption of Pt Species on the CeO_2 Surface. $CeO_2(100)$ nanocubes were synthesized using a supercritical
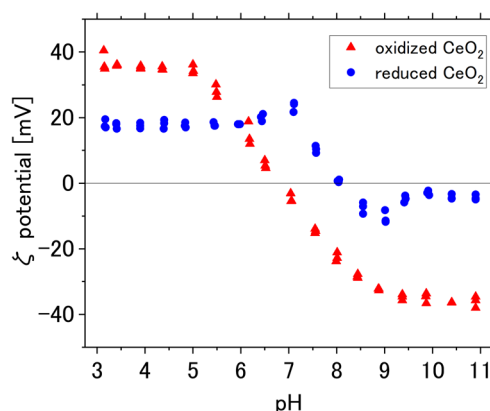
Figure 1. ζ Potentials of oxidized CeO_2, where the point of zero charge is 6.81, and reduced CeO_2, where the point of zero charge is 8.08.

hydrothermal method that involved modifying nanocube surfaces with decanoic acid. The decanoic-acid-modified $CeO_2(100)$ nanocubes were calcined at 300 °C for 2 h in the air to remove the decanoic acid from the surface, resulting in oxidized CeO_2. This produced oxidized CeO_2 was treated at
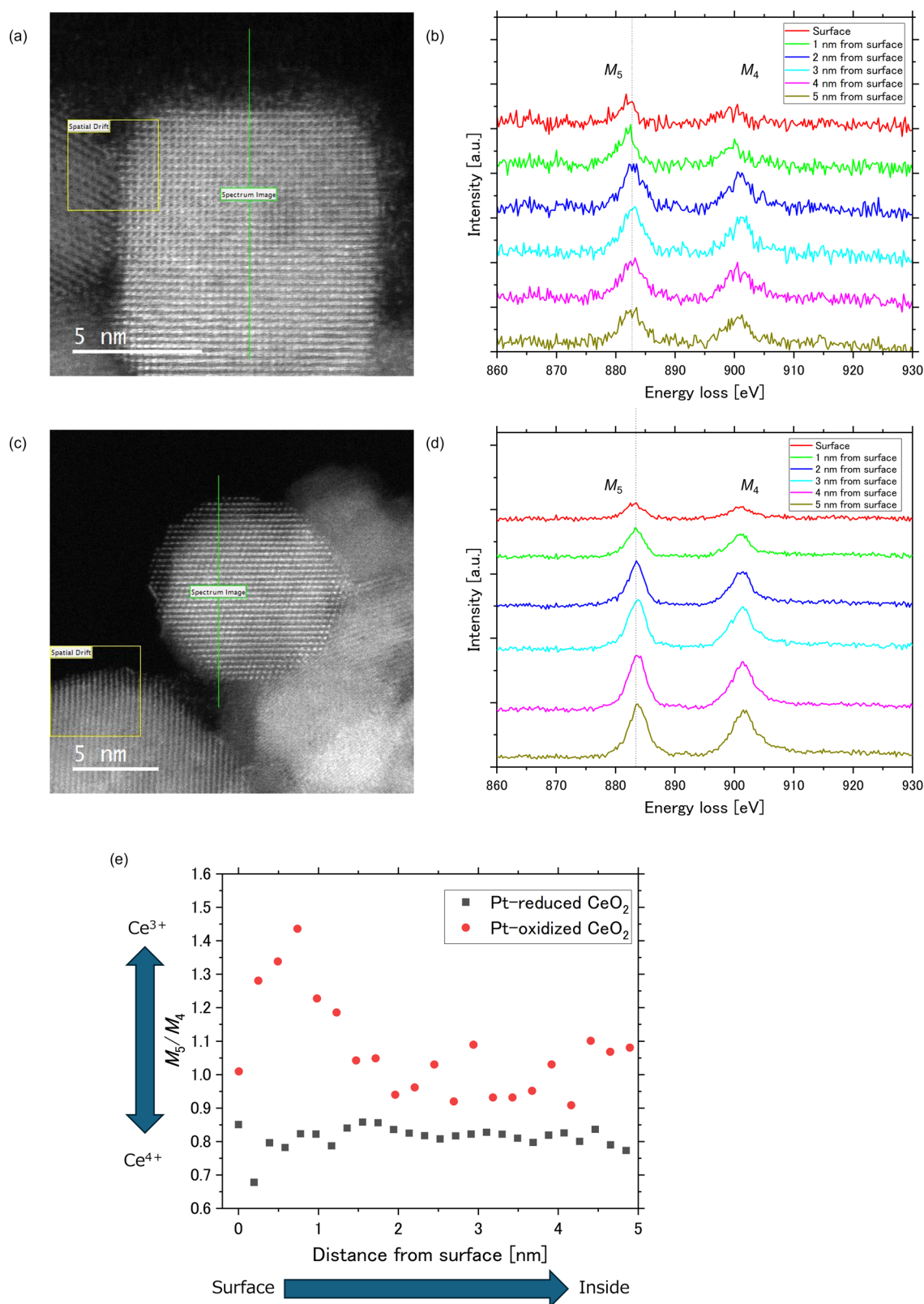
Figure 2. STEM images of (a) Pt-oxidized and (c) Pt-reduced CeO_2. Representative EELS profiles of (b) Pt-oxidized and (d) Pt-reduced CeO_2 at different positions from the surface. (e) Ce valence analysis based on the EELS line scanning. The peak intensity ratios of Ce M_5 and M_4 core loss edges are plotted along the scanning line (shown with the green lines in (a) and (c)) from the surface to the interior to illustrate the chemical state of the Ce ions.

400 °C under a 7% H_2 atmosphere for 2 h to produce reduced CeO_2. For oxidized and reduced CeO_2, Pt was loaded into aqueous solutions to achieve a high degree of surface

dispersion. Figure S1 shows the Pt chemical species at different pH levels for the H_2PtCl_6 starting material. At pH > 5, $Pt(OH)_2$ precipitation occurred. By contrast, Pt existed in

(a)

(b)
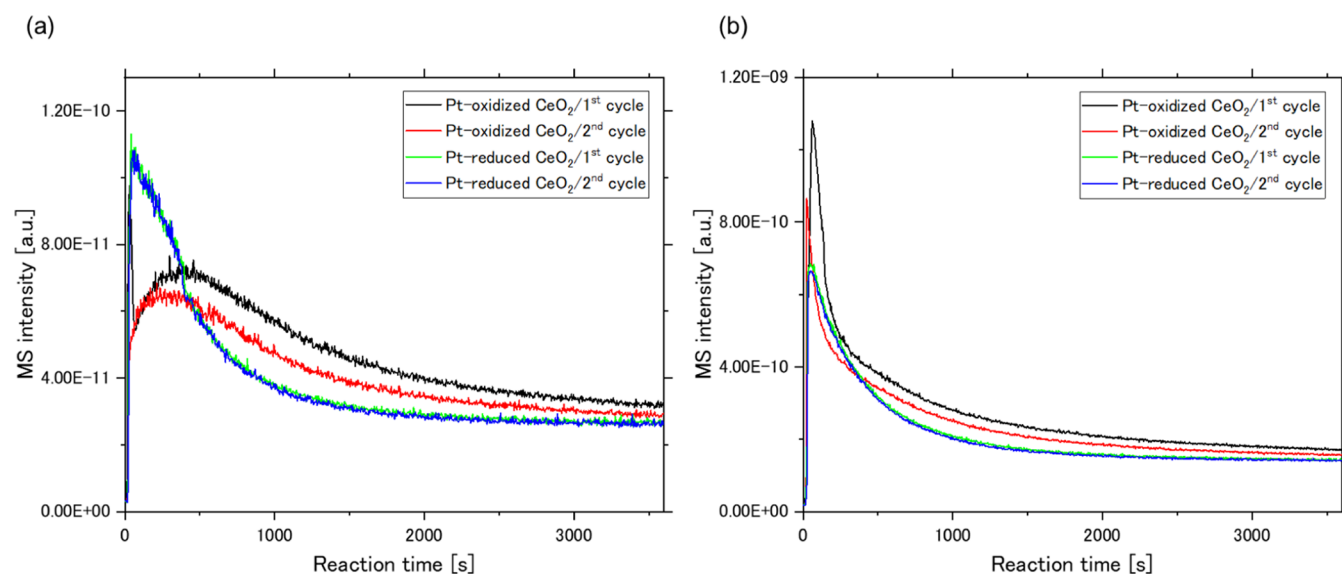
Figure 3. Gas products in the CH_4 reforming steps for two types of $Pt-CeO_2$: (a) CO and (b) H_2.

ionic states at pH < 5. Figure 1 shows the ζ potentials of oxidized and reduced $CeO_2(100)$ nanocubes, revealing their different isoelectric points (6.81 and 8.08, respectively). The results indicated that the differences in their surface natures were maintained even after water immersion. Under low-pH conditions, Pt existed in an ionic state (Figure S1), and both oxidized and reduced CeO_2 possessed positive surface charges when dispersed in water (Figure 1). Pt adsorption was conducted at pH 3 with the main dissolved Pt species, $PtCl_6^{2-}$ and $PtCl_5^-$, which were expected to be efficiently adsorbed onto positively charged CeO_2 surfaces. Subsequently, both samples were recovered via centrifugation and calcined in the air at 300 °C for 12 h to remove chlorine. The introduced amount of Pt was set at 1.0 wt % of the CeO_2 particles, whereas the loaded amount of Pt was 1.0 wt % for oxidized CeO_2 and 0.5 wt % for reduced CeO_2 according to ICP-AES measurements. These amounts corresponded to 0.30 and 0.15 atoms-Pt/nm^2-CeO_2, respectively, as estimated using a cube with a side length of 8 nm.

Figure 2a,c shows high-angular annular dark-field (HAADF) images acquired via STEM of Pt-loaded oxidized and reduced CeO_2. Pt was well dispersed on reduced CeO_2 (Figure S2), as revealed by energy-dispersive X-ray spectroscopy (EDS). No large Pt clusters (with a size on the order of nanometers) were observed for Pt-reduced CeO_2. However, variations depending on the observation spot were observed for Pt-oxidized CeO_2 (Figure S2), suggesting that more aggregation occurred on the oxidized CeO_2 surface than on the reduced CeO_2 surface. Ce valence states were analyzed by using EELS line-scanning measurements of Ce$-M_5$ and M_4 peaks in the core loss edges. Figure 2b,d presents representative EELS spectra for atomic columns from the surface to the interior of the particle. Additional atomic column spectra are shown in Figure S3. The peak intensity ratio of I_{M_5}/I_{M_4} was calculated after extracting the background signal to reveal the valence state. Figure 2e shows the chemical states of both Pt-reduced and Pt-oxidized CeO_2, as evaluated from the EELS peak ratio. Pt-oxidized CeO_2 exhibited more Ce^{3+} ions on its surface, but Ce^{4+} ions were dominant inside the particles, similar to the case of pure CeO_2 nanocubes without metal loading.[30] Interestingly, Pt-reduced CeO_2 had a more oxidized surface than Pt-oxidized

CeO_2, indicating strong interactions between Pt and reduced CeO_2. Hence, electron transfer occurred between the Pt species and the reduced CeO_2 surface.

CH_4 and $Pt-CeO_2$ Reactions. The reactivity of the two $Pt-CeO_2$ samples was examined with chemical looping methane combustion as follows

$$CH_4 + (Pt - CeO_2) \rightarrow CO + 2H_2 + (Pt - CeO_{2-x}) \tag{1}$$

$$(Pt - CeO_{2-x}) + O_2 \rightarrow (Pt - CeO_2) \tag{2}$$
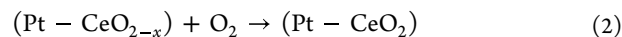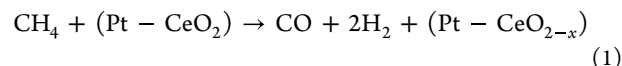
Two cycles of these reactions were conducted for each $Pt-CeO_2$ oxygen-carrier sample (Figure S4). Figure 3 shows the time dependence of CO and H_2—the main products of CH_4 reforming (Reaction 1). The temperature for both reactions was 400 °C, and oxygen was supplied during heating and oxidation prior to the CH_4 reaction. Ar was supplied for gas replacement inbetween Reactions 1 and 2 (Figure S4). The reaction of CH_4 with $Pt-CeO_2$ (Reaction 1) was performed without any additional oxygen supply. As shown in Figure 3, the quantity of gas products decreased over time, owing to the depletion of oxygen from the $Pt-CeO_2$ particles. Hence, gas production reflects the rate of the reaction between CH_4 and oxygen from the $Pt-CeO_2$ particles. Notably, Pt-oxidized and Pt-reduced CeO_2 exhibited substantially different reactivities, with the latter being considerably higher. Furthermore, a significant difference was observed in their stabilities. For Pt-reduced CeO_2, the reaction was repeated without significant deterioration, whereas poor cyclability was observed for Pt-oxidized CeO_2. Slight changes in the loading process, i.e., with and without reduction pretreatment, clearly affected the reactivity and stability of these oxygen carriers.

Atomistic Insight into $Pt-CeO_2$ Particles. To gain a more detailed understanding of the reactivity and stability differences in $Pt-CeO_2$ nanoparticles as oxygen carriers, in situ XAFS was employed. Figure 4 presents the Pt L_3-edge XAFS data, with Figure 4a,b showcasing the X-ray absorption near edge spectra (XANES) and Fourier transform magnitudes from the extended X-ray absorption fine structure (EXAFS) data for the initial states of Pt-oxidized and Pt-reduced CeO_2 in comparison with reference samples. The XANES spectra
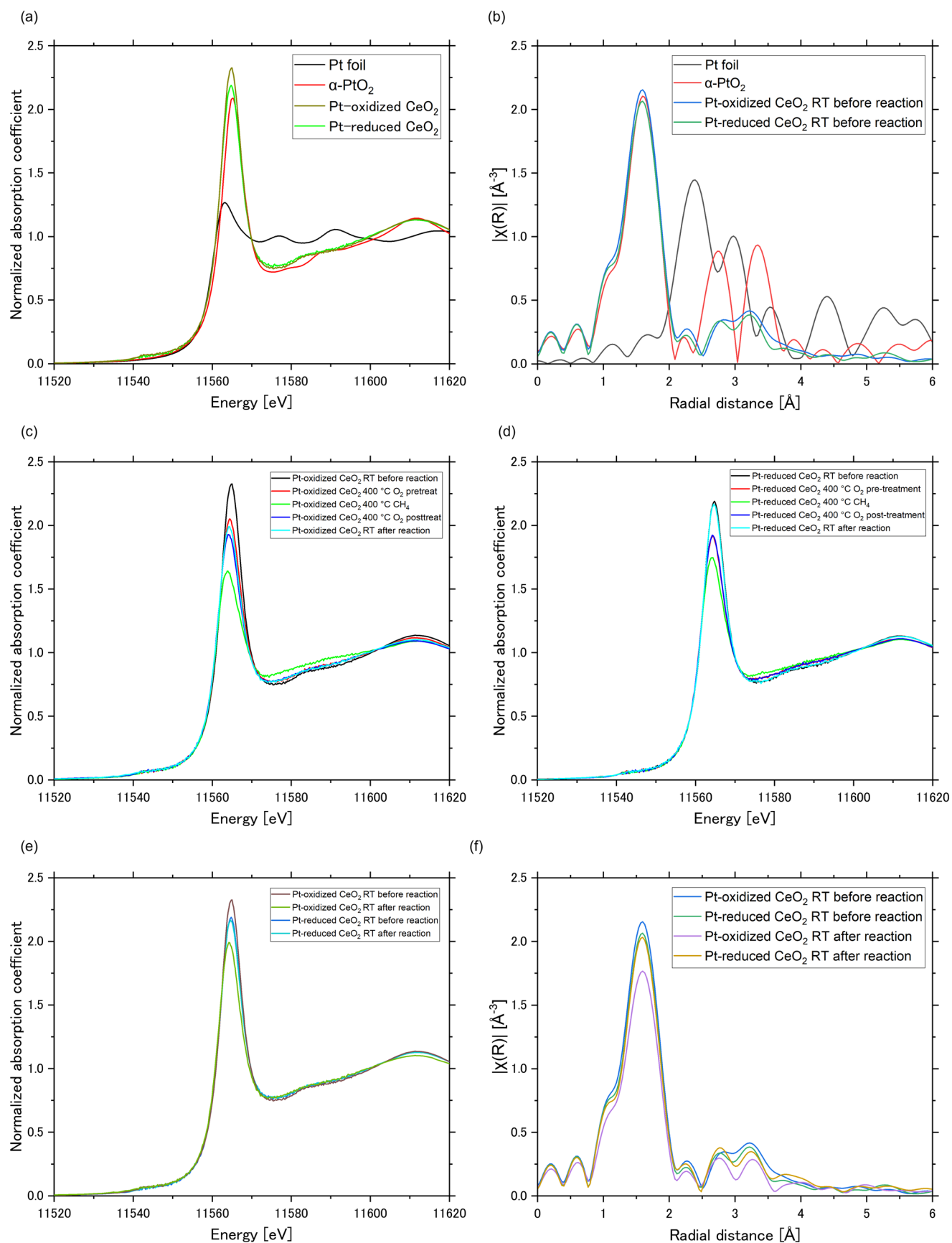
Figure 4. In situ XAFS spectra: (a) Pt L_3-edge XANES spectra of the initial state of samples compared with references; (b) Pt L_3-edge Fourier transform magnitude obtained from EXAFS for the initial states of samples compared with references; (c) in situ Pt L_3-edge XANES spectra of Pt-oxidized CeO_2 nanoparticles for CH_4 reforming at 400 °C; (d) in situ Pt L_3-edge XANES spectra of Pt-reduced CeO_2 nanoparticles for CH_4

Figure 4. continued

reforming at 400 °C; (e) comparison of Pt L_3-edge XANES spectra of Pt-oxidized CeO_2 and Pt-reduced CeO_2 nanoparticles before and after the reaction; (f) comparison of Pt L_3-edge Fourier transform magnitudes based on EXAFS for Pt-oxidized CeO_2 and Pt-reduced CeO_2 nanoparticles.
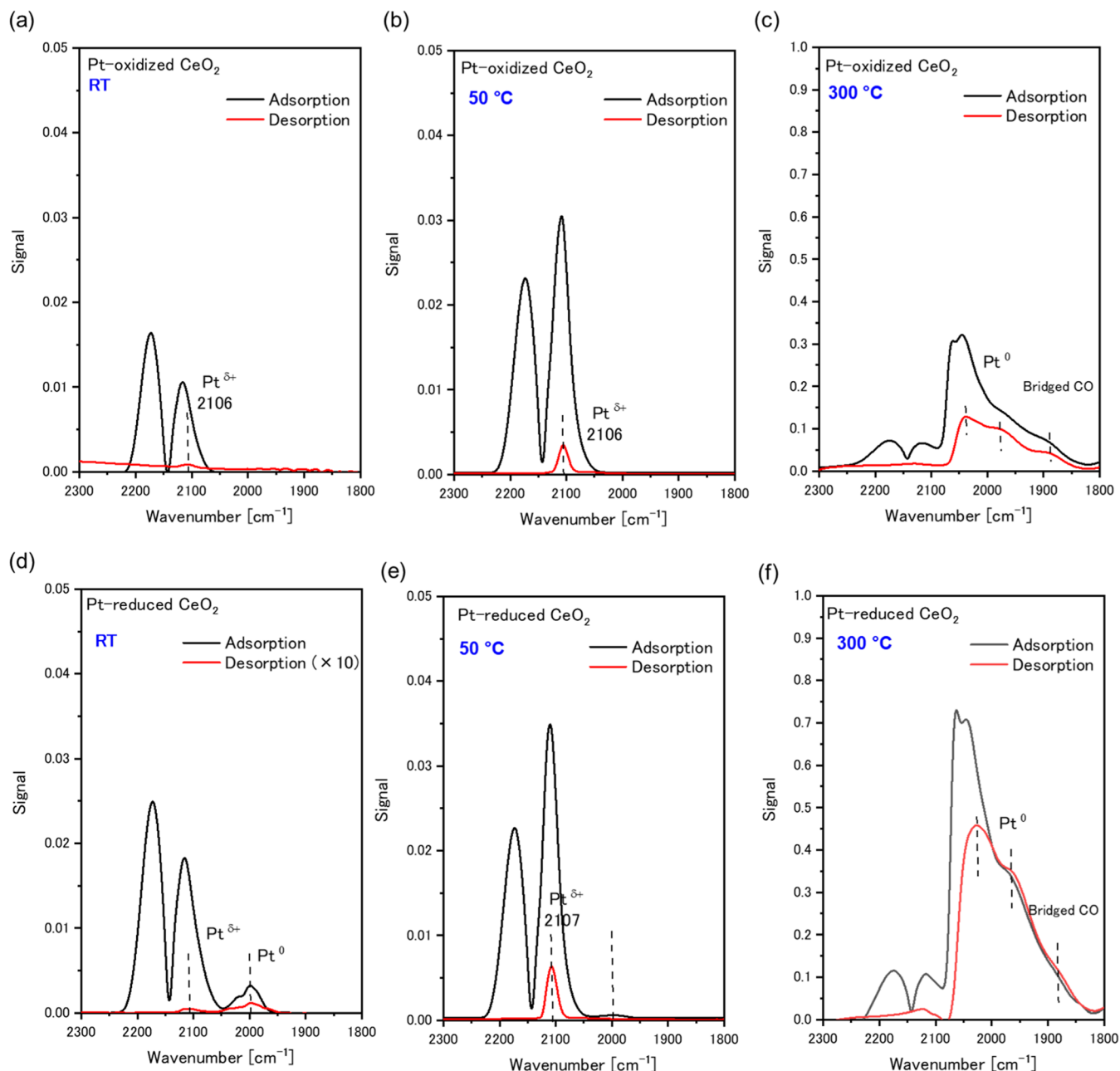

Figure 5. DRIFTS measurement data for adsorption and desorption of CO during the heating of Pt-oxidized CeO_2 ((a) RT, (b) 50 °C, (c) 300 °C) and Pt-reduced CeO_2 ((d) RT, (e) 50 °C, (f) 300 °C).

indicated the existence of Pt at a more reduced charge state in these samples compared with the PtO_2 reference, which was inferred from the lower-energy peaks. Additionally, a minor difference was noted between the oxidized and reduced CeO_2 samples in the XANES spectra. The EXAFS data revealed Pt–O bonds similar to those in Pt oxide but with a notably weak second coordination (Pt–O–M(Pt, Ce)) peak, suggesting significant disorder in the local Pt structure. The predominant Pt^{2+} chemical state in both samples, along with the slight

variation between them, was confirmed by ex situ XPS (Figure S5).

After the reaction cell was heated to 400 °C in an O_2 atmosphere, a methane reaction was conducted on Pt-oxidized and Pt-reduced CeO_2 samples. The Pt L_3-edge spectra, as illustrated in Figure 4c,d, exhibited a reduction in white-line intensities post-CH_4 reaction, indicating oxygen consumption near Pt for CH_4 oxidation. Subsequent reoxidation with O_2 confirmed the oxidation states. However, Pt-oxidized CeO_2 did not revert to its initial chemical state, suggesting an irreversible
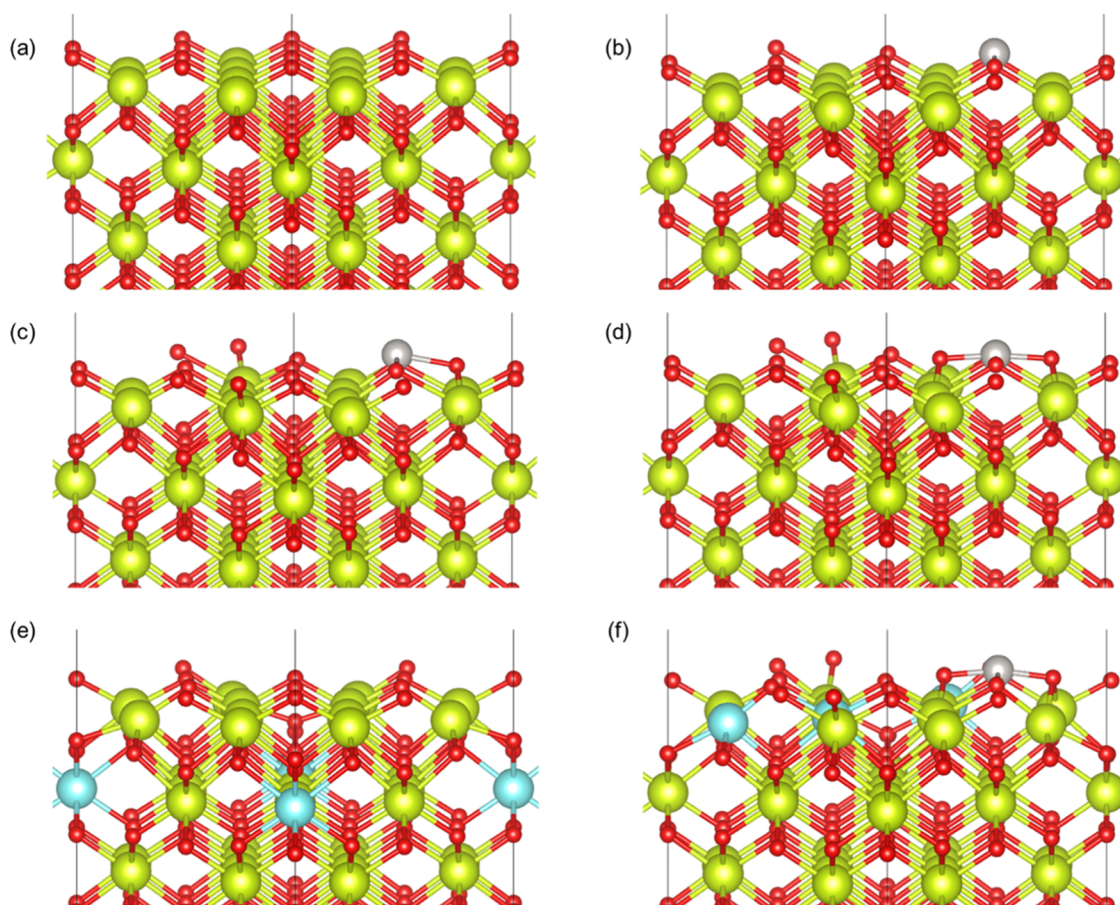
Figure 6. DFT simulations of Pt-loaded CeO_2: (a) pure stoichiometry $CeO_2(100)$ facet; (b) Pt atom placement on stoichiometric $CeO_2(100)$; (c) Pt−O molecule placement on stoichiometric $CeO_2(100)$; (d) PtO_2 molecule placement on stoichiometric $CeO_2(100)$; (e) $CeO_2(100)$ facet with an oxygen vacancy; and (f) PtO_2 molecule placement on $CeO_2(100)$ with an oxygen vacancy in the subsurface layer. Light green, sky blue, red, and gray balls represent Ce^{4+} ions, Ce^{3+} ions, O atoms, and Pt atoms, respectively.

change in the state of Pt, i.e., its dispersibility/aggregation on CeO_2 particles (For pure CeO_2 nanoparticles, reduction and reoxidation cycles are reversible at this temperature.[30,31,33,34]). By contrast, Pt-reduced CeO_2 exhibited a distinct restoration of the Pt chemical states, as shown in Figure 4d. This stability in the dispersed Pt state was likely due to robust interactions between Pt and the reduced CeO_2 surface, which is rich in Ce^{3+} ions and oxygen vacancies initially, facilitating the reversion to original chemical configurations.

The in situ XAFS spectra—particularly the XANES (Figure 4e) and EXAFS (Figure 4f) data—were pivotal in discerning the reaction behaviors between Pt-reduced and Pt-oxidized samples. The minimal spectral changes observed in the Pt-reduced CeO_2 sample relative to the Pt-oxidized CeO_2 sample suggest that the Pt species interacted strongly with oxygen vacancies and contributed to the reversibility of the Pt-reduced CeO_2 sample during the CH_4 reaction. This interaction is evidenced by the consistency between the ex situ XPS results (Figure S5) and the in situ XAFS data. The slight differences in the chemical state and dispersibility of the Pt species significantly affected the reactivity and stability of the samples.

To examine the chemical state of Pt on CeO_2, DRIFTS analysis was performed, with a focus on CO adsorption and desorption as can be seen in Figure 5. At room temperature (RT), there was a noticeable difference between Pt-oxidized CeO_2 and Pt-reduced CeO_2. The reduced sample exhibited two CO adsorption states. Regarding $Pt^{\delta+}$, the peak at 2107

cm^{-1} was assigned to linearly adsorbed CO on positively charged Pt. Regarding Pt^0, the peak at $2000-2100$ cm^{-1} was assigned to linearly adsorbed CO on Pt^0. Notably, the oxidized sample had only a $Pt^{\delta+}$ state, which is consistent with those detected by XAFS and XPS, where slight reductive shifts were observed for Pt-reduced CeO_2. With an increase in the temperature, the fraction of Pt^0-assigned species increased significantly, and a higher adsorption intensity was observed for Pt-reduced CeO_2. This increase in Pt^0 species and higher intensity suggest the enhanced reactivity of surface oxygen, indicating a more rapid consumption of O_2 in the Pt-reduced CeO_2. The difference in the reactivity was also supported by temperature-programmed reduction with CO (Figure S6).

Interaction between Pt and Reduced CeO_2(100) Surface. The interaction between the Pt species and the reduced $CeO_2(100)$ surface significantly influenced the material's reactivity and stability. This interaction was studied by using density functional theory (DFT) simulations. Figure 6 presents the simulated models of the $CeO_2(100)$ surface, emphasizing its polar characteristics. To accurately represent stoichiometric CeO_2, oxygen atoms were symmetrically placed on both sides of the slab model, neutralizing the surface's inherent polarity (Figure 6a). Bader charge analysis revealed that the initial charge of the first Ce layer in (100) CeO_2 was +2.37 lel. When a Pt atom was placed on this surface layer, the Bader charges of Ce and Pt were +2.34 lel and +0.26 lel, respectively (Figure 6b). Upon the introduction of additional

oxygen to platinum on the CeO_2 surface, which formed PtO and PtO_2 with formal charges of +2 and +4, the Bader charges for Pt were observed to be +0.73 |e| for PtO and +1.29 |e| for PtO_2, as illustrated in Figure 6c,d, respectively. In comparison, the bulk Bader charges for PtO and PtO_2 were higher, i.e., + 0.91 |e| and +1.67 |e|, respectively, indicating a variation in electronic states between surface-bound and bulk platinum–oxygen configurations. The interaction of Pt with the CeO_2 surface led to a reductive shift in Pt's electronic state. Additionally, when an oxygen vacancy formed in the subsurface layer of pure CeO_2, two Ce^{3+} (Bader charge: + 2.15 |e|, this is consistent with previous findings on bulk reduced CeO_2[31]) polarons were observed in the subsurface layer (Figure 6e). The presence of an oxygen vacancy in the subsurface layer of CeO_2 with PtO_2 on the surface altered the electronic structure, as evidenced by the Bader charges of Pt (1.08 |e|) and the two Ce^{3+} polarons (+2.20 |e|; Figure 6f), indicating slight electron transfer from Ce to Pt. This interaction reduced the oxygen vacancy formation energy of the stoichiometric (100) subsurface from 0.84 eV in pure CeO_2 (Figure 6e) to 0.64 eV with Pt (Figure 6f), enhancing the reducibility of the CeO_2 surface and stabilizing its reduced state.

CONCLUSIONS

The proposed methodology featuring reduction pretreatment is promising for creating highly active and stable Pt-loaded CeO_2. The significant interactions between Pt species and reduced CeO_2 enhance the Pt dispersibility and chemical states, as demonstrated by methane chemical looping. The strong interaction between Pt and reduced CeO_2 was elucidated based on first-principles simulations, which revealed that Pt stabilizes oxygen vacancies on the CeO_2 surface, thereby significantly reducing the energy needed to form these vacancies compared with pure CeO_2. This stabilization contributes to the reactivity and stability of the system, as evidenced by in situ XAFS and DRIFTS data with a focus on the chemical state of Pt on the CeO_2(100) surface. By precisely controlling the size, shape, and redox state of CeO_2 nanoparticles, the effectiveness of noble-metal catalysts can be optimized, reducing the amount of precious metal required and enhancing the catalyst performance.

ASSOCIATED CONTENT

Supporting Information

The Supporting Information is available free of charge at https://pubs.acs.org/doi/10.1021/acs.chemmater.4c00627.

Pt species solubility calculations, STEM-EDS maps, Ce M_4 and M_5 EELS profiles, reaction cycle diagrams, Pt 4f XPS profiles, and CO-TPR results (PDF)

AUTHOR INFORMATION

Corresponding Authors

Akira Yoko − *WPI-Advanced Institute for Materials Research (WPI-AIMR), Tohoku University, Sendai 980-8577, Japan; International Center for Synchrotron Radiation Innovation Smart (SRIS), Tohoku University, Sendai 980-8572, Japan;* orcid.org/0000-0002-1278-272X; Email: akira.yoko.c7@tohoku.ac.jp

Anatoly I. Frenkel − *Department of Materials Science and Chemical Engineering, Stony Brook University, Stony Brook, New York 11794, United States; Chemistry Division, Brookhaven National Laboratory, Upton, New York 11973, United States;* orcid.org/0000-0002-5451-1207; Email: anatoly.frenkel@stonybrook.edu

Yuichi Ikuhara − *WPI-Advanced Institute for Materials Research (WPI-AIMR), Tohoku University, Sendai 980-8577, Japan; Institute of Engineering Innovation, The University of Tokyo, Tokyo 113-8656, Japan;* orcid.org/0000-0003-3886-005X; Email: ikuhara@sigma.t.u-tokyo.ac.jp

Tadafumi Adschiri − *WPI-Advanced Institute for Materials Research (WPI-AIMR), Tohoku University, Sendai 980-8577, Japan; New Industry Creation Hatchery Center, Tohoku University, Sendai 980-8579, Japan;* Email: tadafumi.ajiri.b1@tohoku.ac.jp

Authors

Haodong Wang − *Department of Materials Science and Chemical Engineering, Stony Brook University, Stony Brook, New York 11794, United States; Chemistry Division, Brookhaven National Laboratory, Upton, New York 11973, United States*

Ko Furuya − *Department of Chemical Engineering, Graduate School of Engineering, Tohoku University, Sendai 980-8577, Japan*

Daiki Takahashi − *Department of Chemical Engineering, Graduate School of Engineering, Tohoku University, Sendai 980-8577, Japan*

Gimyeong Seong − *Department of Environmental & Energy Engineering, The University of Suwon, Hwaseong-si 18323 Gyeonggi-do, Republic of Korea;* orcid.org/0000-0003-4292-5936

Takaaki Tomai − *Institute of Multidisciplinary Research for Advanced Materials, Tohoku University, Sendai 980-8577, Japan; Frontier Research Institute for Interdisciplinary Sciences, Tohoku University, Sendai 980-8578, Japan;* orcid.org/0000-0003-0296-6565

Mitsuhiro Saito − *Institute of Engineering Innovation, The University of Tokyo, Tokyo 113-8656, Japan;* orcid.org/0000-0003-1602-0308

Kazutoshi Inoue − *WPI-Advanced Institute for Materials Research (WPI-AIMR), Tohoku University, Sendai 980-8577, Japan*

Complete contact information is available at:
https://pubs.acs.org/10.1021/acs.chemmater.4c00627

Author Contributions

The manuscript was written through contributions of all authors. All authors have given approval to the final version of the manuscript.

Notes

The authors declare no competing financial interest.

ACKNOWLEDGMENTS

■ REFERENCES

(1) Zhou, Y.; Xi, W.; Xie, Z.; You, Z.; Jiang, X.; Han, B.; Lang, R.; Wu, C. High-Loading Pt Single-Atom Catalyst on CeO$_2$-Modified Diatomite Support. *Chem. - Asian J.* 2021, 16, 2622−2625.

(2) Liu, L.; Das, S.; Zhang, Z.; Kawi, S. Nonoxidative Coupling of Methane Over Ceria-Supported Single-Atom Pt Catalysts in DBD Plasma. *ACS Appl. Mater. Interfaces* 2022, 14, 5363−5375.

(3) Shen, D.; Li, Z.; Shan, J.; Yu, G.; Wang, X.; Zhang, Y.; Liu, C.; Lyu, S.; Li, J.; Li, L. Synergistic Pt−CeO$_2$ Interface Boosting Low Temperature Dry Reforming of Methane. *Appl. Catal., B* 2022, 318, No. 121809.

(4) Qi, H.; Yang, J.; Liu, F.; Zhang, L.; Yang, J.; Liu, X.; Li, L.; Su, Y.; Liu, Y.; Hao, R.; Wang, A.; Zhang, T. Highly Selective and Robust Single-Atom Catalyst Ru$_1$/NC for Reductive Amination of Aldehydes/Ketones. *Nat. Commun.* 2021, 12, No. 3295.

(5) Zhang, K.; Meng, Q.; Wu, H.; Yan, J.; Mei, X.; An, P.; Zheng, L.; Zhang, J.; He, M.; Han, B. Selective Hydrodeoxygenation of Aromatics to Cyclohexanols Over Ru Single Atoms Supported on CeO$_2$. *J. Am. Chem. Soc.* 2022, 144, 20834−20846.

(6) Zheng, K.; Li, Y.; Liu, B.; Jiang, F.; Xu, Y.; Liu, X. Ti-Doped CeO$_2$ Stabilized Single-Atom Rhodium Catalyst for Selective and Stable CO$_2$ Hydrogenation to Ethanol. *Angew. Chem., Int. Ed.* 2022, 61, No. e202210991.

(7) Xie, S.; Kim, D.; Ye, K.; Tetard, L.; Liu, F. Regulating Local Coordination Environment of Rhodium Single Atoms in Rh/CeO$_2$ Catalysts for N$_2$O Decomposition. *J. Rare Earths* 2023, 41, 941−951.

(8) Zheng, Y.; Wang, Q.; Yang, Q.; Wang, S.; Hülsey, M. J.; Ding, S.; Furukawa, S.; Li, M.; Yan, N.; Ma, X. Boosting the Hydroformylation Activity of a Rh/CeO$_2$ Single-Atom Catalyst by Tuning Surface Deficiencies. *ACS Catal.* 2023, 13, 7243−7255.

(9) Muravev, V.; Spezzati, G.; Su, Y.-Q.; Parastaev, A.; Chiang, F.-K.; Longo, A.; Escudero, C.; Kosinov, N.; Hensen, E. J. M. Interface Dynamics of Pd−CeO$_2$ Single-Atom Catalysts During CO Oxidation. *Nat. Catal.* 2021, 4, 469−478.

(10) Vice, A.; Langer, N.; Reinhart, B.; Kedem, O. Surface-Modified Pd/CeO$_2$ Single-Atom Catalyst Shows Increased Activity for Suzuki Cross-Coupling. *Inorg. Chem.* 2023, 62, 21479−21486.

(11) Wu, J.; Wu, Y.; Lu, L.; Zhang, D.; Wang, X. Single-Atom Au Catalyst Loaded on CeO$_2$, A Novel Single-Atom Nanozyme Electrochemical H$_2$O$_2$ Sensor. *Talanta Open* 2021, 4, No. 100075.

(12) Liang, Y.; Wu, C.; Meng, S.; Lu, Z.; Zhao, R.; Wang, H.; Liu, Z.; Wang, J. Ag Single Atoms Anchored on CeO$_2$ with Interfacial

(13) Bunluesin, T.; Putna, E. S.; Gorte, R. J. A Comparison of CO Oxidation on Ceria-Supported Pt, Pd, and Rh. *Catal. Lett.* 1996, 41, 1−5.

(14) Bunluesin, T.; Gorte, R. J.; Graham, G. W. Studies of the Water-Gas-Shift Reaction on Ceria-Supported Pt, Pd, and Rh: Implications for Oxygen-Storage Properties. *Appl. Catal., B* 1998, 15, 107−114.

(15) Holmgren, A.; Andersson, B. Oxygen Storage Dynamics in Pt/CeO$_2$/Al$_2$O$_3$ Catalysts. *J. Catal.* 1998, 178, 14−25.

(16) Pereira-Hernández, X. I.; DeLaRiva, A.; Muravev, V.; Kunwar, D.; Xiong, H.; Sudduth, B.; Engelhard, M.; Kovarik, L.; Hensen, E. J. M.; Wang, Y.; Datye, A. K. Tuning Pt-CeO$_2$ Interactions by High-Temperature Vapor-Phase Synthesis for Improved Reducibility of Lattice Oxygen. *Nat. Commun.* 2019, 10, No. 1358.

(17) Zeng, L.; Cheng, Z.; Fan, J. A.; Fan, L.-S.; Gong, J. Metal Oxide Redox Chemistry for Chemical Looping Processes. *Nat. Rev. Chem.* 2018, 2, 349−364.

(18) Kraushofer, F.; Parkinson, G. S. Single-Atom Catalysis: Insights from Model Systems. *Chem. Rev.* 2022, 122, 14911−14939.

(19) Saptal, V. B.; Ruta, V.; Bajada, M. A.; Vilé, G. Single-Atom Catalysis in Organic Synthesis. *Angew. Chem., Int. Ed.* 2023, 62, No. e202219306.

(20) Kottwitz, M.; Li, Y.; Wang, H.; Frenkel, A. I.; Nuzzo, R. G. Single Atom Catalysts: A Review of Characterization Methods. *Chem. Methods* 2021, 1, 278−294.

(21) Kottwitz, M.; Li, Y.; Palomino, R. M.; Liu, Z.; Wang, G.; Wu, Q.; Huang, J.; Timoshenko, J.; Senanayake, S. D.; Balasubramanian, M.; Lu, D.; Nuzzo, R. G.; Frenkel, A. I. Local Structure and Electronic State of Atomically Dispersed Pt Supported on Nanosized CeO$_2$. *ACS Catal.* 2019, 9, 8738−8748.

(22) Daelman, N.; Capdevila-Cortada, M.; López, N. Dynamic Charge and Oxidation State of Pt/CeO$_2$ Single-Atom Catalysts. *Nat. Mater.* 2019, 18, 1215−1221.

(23) Wang, H.; Kottwitz, M.; Rui, N.; Senanayake, S. D.; Marinkovic, N.; Li, Y.; Nuzzo, R. G.; Frenkel, A. I. Aliovalent Doping of CeO$_2$ Improves the Stability of Atomically Dispersed Pt. *ACS Appl. Mater. Interfaces* 2021, 13, 52736−52742.

(24) Feng, Y.; Wan, Q.; Xiong, H.; Zhou, S.; Chen, X.; Hernandez, X. I. P.; Wang, Y.; Lin, S.; Datye, A. K.; Guo, H. Correlating DFT Calculations with CO Oxidation Reactivity on Ga-Doped Pt/CeO$_2$ Single-Atom Catalysts. *J. Phys. Chem. C* 2018, 122, 22460−22468.

(25) Tao, Q.; Song, J.; Sun, N.; Ren, Y.; Xiang, L.; Liu, S.; Kuai, L. Boosting the Activity of Single-Atom Pt$_1$/CeO$_2$ via Co Doping for Low-Temperature Catalytic Oxidation of CO. *Inorg. Chem.* 2022, 61, 11932−11938.

(26) Li, Y.; Kottwitz, M.; Vincent, J. L.; Enright, M. J.; Liu, Z.; Zhang, L.; Huang, J.; Senanayake, S. D.; Yang, W.-C. D.; Crozier, P. A.; Nuzzo, R. G.; Frenkel, A. I. Dynamic Structure of Active Sites in Ceria-Supported Pt Catalysts for the Water Gas Shift Reaction. *Nat. Commun.* 2021, 12, No. 914.

(27) Zhang, Z.; Tian, J.; Lu, Y.; Yang, S.; Jiang, D.; Huang, W.; Li, Y.; Hong, J.; Hoffman, A. S.; Bare, S. R.; Engelhard, M. H.; Datye, A. K.; Wang, Y. Memory-Dictated Dynamics of Single-Atom Pt on CeO$_2$ for CO Oxidation. *Nat. Commun.* 2023, 14, No. 2664.

(28) Zhang, J.; Ohara, S.; Umetsu, M.; Naka, T.; Hatakeyama, Y.; Adschiri, T. Colloidal Ceria Nanocrystals: A Tailor-Made Crystal Morphology in Supercritical Water. *Adv. Mater.* 2007, 19, 203−206.

(29) Zhang, J.; Kumagai, H.; Yamamura, K.; Ohara, S.; Takami, S.; Morikawa, A.; Shinjoh, H.; Kaneko, K.; Adschiri, T.; Suda, A. Extra-Low-Temperature Oxygen Storage Capacity of CeO$_2$ Nanocrystals with Cubic Facets. *Nano Lett.* 2011, 11, 361−364.

(30) Hao, X.; Yoko, A.; Chen, C.; Inoue, K.; Saito, M.; Seong, G.; Takami, S.; Adschiri, T.; Ikuhara, Y. Atomic-Scale Valence State Distribution Inside Ultrafine CeO$_2$ Nanocubes and Its Size Dependence. *Small* 2018, 14, No. e1802915.

(31) Hao, X. D.; Yoko, A.; Inoue, K.; Xu, Y.; Saito, M.; Chen, C.; Seong, G.; Tomai, T.; Takami, S.; Shluger, A. L.; Xu, B. S.; Adschiri,

T.; Ikuhara, Y. Atomistic Origin of High-Concentration Ce^{3+} in {100}-Faceted Cr-Substituted CeO_2 Nanocrystals. *Acta Mater.* **2021**, *203*, No. 116473.

(32) Omura, Y.; Yoko, A.; Seong, G.; Nishibori, M.; Ninomiya, K.; Tomai, T.; Adschiri, T. Uniform Organically Modified CeO_2 Nanoparticles Synthesized from a Carboxylate Complex Under Supercritical Hydrothermal Conditions: Impact of Ce Valence. *J. Phys. Chem. C* **2022**, *126*, 6008−6015.

(33) Seong, G.; Yoko, A.; Inoue, R.; Takami, S.; Adschiri, T. Selective Chemical Recovery from Biomass Under Hydrothermal Conditions Using Metal Oxide Nanocatalyst. *J. Supercrit. Fluids* **2018**, *133*, 726−737.

(34) Yoko, A.; Fukushima, Y.; Shimizu, T.; Kikuchi, Y.; Shimizu, T.; Guzman-Urbina, A.; Ouchi, K.; Hirai, H.; Seong, G.; Tomai, T.; Adschiri, T. Process Assessments for Low-Temperature Methane Reforming Using Oxygen Carrier Metal Oxide Nanoparticles. *Chem. Eng. Process.* **2019**, *142*, No. 107531.

(35) Zhu, Y.; Seong, G.; Noguchi, T.; Yoko, A.; Tomai, T.; Takami, S.; Adschiri, T. Highly Cr-Substituted CeO_2 Nanoparticles Synthesized Using a Non-equilibrium Supercritical Hydrothermal Process: High Oxygen Storage Capacity Materials Designed for a Low-Temperature Bitumen Upgrading Process. *ACS Appl. Energy Mater.* **2020**, *3*, 4305−4319.

(36) Yoko, A.; Kamonvarapitak, T.; Seong, G.; Tomai, T.; Adschiri, T. Supercritical Hydrothermal Synthesis of Organic-Modified $Ce_{1-x}Zr_xO_{2-\delta}$ ($0 \leq x \leq 1$) Nanoparticles as a Low-Temperature Oxygen Carrier. *ChemNanoMat* **2022**, *8*, No. e202100495.

(37) Yoko, A.; Seong, G.; Tomai, T.; Adschiri, T. Continuous Flow Synthesis of Nanoparticles Using Supercritical Water: Process Design, Surface Control, and Nanohybrid Materials. *KONA Powder Part. J.* **2020**, *37*, 28−41.

(38) Seong, G.; Aida, T.; Nakagawa, Y.; Nanba, T.; Okada, O.; Yoko, A.; Tomai, T.; Takami, S.; Adschiri, T. Fabrication of FeO_x-ZrO_2 Nanostructures for Automotive Three-Way Catalysts by Supercritical Hydrothermal Synthesis with Supercritical CO_2 Drying. *J. Supercrit. Fluids* **2019**, *147*, 302−309.

(39) Seong, G.; Dejhosseini, M.; Adschiri, T. A kinetic study of catalytic hydrothermal reactions of acetaldehyde with cubic CeO_2 nanoparticles. *Appl. Catal., A* **2018**, *550*, 284−296.

(40) Kresse, G.; Furthmuller, J. Efficient Iterative Schemes for *Ab Initio* Total-Energy Calculations Using a Plane-Wave Basis Set. *Phys. Rev. B* **1996**, *54*, 11169−11186.

(41) Kresse, G.; Joubert, D. From Ultrasoft Pseudopotentials to the Projector Augmented-Wave Method. *Phys. Rev. B* **1999**, *59*, 1758−1775.

(42) Perdew, J. P.; Burke, K.; Ernzerhof, M. Generalized Gradient Approximation Made Simple. *Phys. Rev. Lett.* **1996**, *77*, 3865−3868.

(43) Dudarev, S. L.; Botton, G. A.; Savrasov, S. Y.; Humphreys, C. J.; Sutton, A. P. Electron-Energy-Loss Spectra and the Structural Stability of Nickel Oxide: An LSDA+*U* Study. *Phys. Rev. B* **1998**, *57*, 1505−1509.

(44) Keating, P. R. L.; Scanlon, D. O.; Morgan, B. J.; Galea, N. M.; Watson, G. W. Analysis of Intrinsic Defects in CeO_2 Using a Koopmans-Like GGA Plus *U* Approach. *J. Phys. Chem. C* **2012**, *116*, 2443−2452.

(45) Yang, Y.; Sugino, O.; Ohno, T. Possible Magnetic Behavior in Oxygen-Deficient β-PtO_2. *Phys. Rev. B* **2012**, *85*, No. 035204.

(46) Makov, G.; Payne, M. C. Periodic Boundary Conditions in *Ab Initio* Calculations. *Phys. Rev. B* **1995**, *51*, 4014−4022.

(47) Neugebauer, J.; Scheffler, M. Adsorbate-Substrate and Adsorbate-Adsorbate Interactions of Na and K Adlayers on Al(111). *Phys. Rev. B* **1992**, *46*, 16067−16080.

(48) Momma, K.; Izumi, F. VESTA. VESTA 3 for Three-Dimensional Visualization of Crystal, Volumetric and Morphology Data. *J. Appl. Crystallogr.* **2011**, *44*, 1272−1276.